Long-scale phase separation versus homogeneous magnetic state in $(\text{La}_{1-y}\text{Pr}_y)_{0.7}\text{Ca}_{0.3}\text{MnO}_3$: A neutron diffraction study

A. M. Balagurov

Frank Laboratory of Neutron Physics, Joint Institute for Nuclear Research, 141980 Dubna, Moscow region, Russia

V. Yu. Pomjakushin*

Laboratory for Neutron Scattering, ETH Zurich and Paul Scherrer Institute, CH-5232 Villigen PSI, Switzerland

D. V. Sheptyakov and V. L. Aksenov

Frank Laboratory of Neutron Physics, Joint Institute for Nuclear Research, 141980 Dubna, Moscow region, Russia

P. Fischer and L. Keller

Laboratory for Neutron Scattering, ETH Zurich and Paul Scherrer Institute, CH-5232 Villigen PSI, Switzerland

O. Yu. Gorbenko and A. R. Kaul

Chemistry Department, Moscow State University, 119899 Moscow, Russia

N. A. Babushkina

RSC ''Kurchatov Institute,'' Kurchatov Square 1, 123182 Moscow, Russia

The magnetic structure of the series $(\text{La}_{1-y}\text{Pr}_y)_{0.7}\text{Ca}_{0.3}\text{MnO}_3$ for y from 0.5 to 1.0 has been studied by neutron powder diffraction in the temperature range from 10 to 293 K and in external magnetic fields up to 4 T. The phase diagram has a border region of concentrations $0.6 \leqslant y \leqslant 0.8$ separating the homogeneous ferromagnetic (FM) metallic and canted antiferromagnetic (AFM) insulating states. In this region the low-temperature magnetic state is macroscopically ($> 10^3$ Å) separated into AFM and FM phases. The FM phase has a small noncollinearity, presumably due to interfaces to the AFM phase. The macroscopical clusters can be induced by disorder on the carrier's hopping amplitude caused by natural dispersion of the A cation radius near the metal-insulator transition around $y = 0.7$. For the concentrations $y \geqslant 0.9$ the long-range ordered magnetic state is homogeneous with a canted AFM structure. The total long-range ordered magnetic moment of the Mn ion shows a steplike decrease from $\mu_{\text{Mn}} = 3.4\mu_B$ to $2.5\mu_B$ as a function of Pr concentration at the transition to a homogeneous canted antiferromagnetic (CAF) state. The spatial inhomogeneities can still be present for $y \geqslant 0.9$, according to the reduced μ_{Mn} value, but the Mn spins between the homogeneously CAF-ordered moments have to be either short-range ordered or paramagnetic. In addition, a ferromagnetic contribution of the Pr moments parallel to the ferromagnetic component of Mn moments is found for $y > 0.6$. The moment of Pr scales with the ferromagnetic Mn moment rather than with the Pr concentration and thus presumably induced by Mn.

I. INTRODUCTION

The perovskite manganites $A_{1-x}A'_x\text{MnO}_3$, where $A = \text{La}$ or other rare earth, $A' = \text{Ca}$, Sr, Ba, have been attracting considerable scientific interest due to rediscovery of the colossal magnetoresistance effect[1] (CMR) and a remarkable interplay of electronic, magnetic, and crystal lattice properties. The magnetoresistance effect in manganites was originally explained in the context of double exchange (DE) of localized t_{2g} Mn^{3+} spins mediated by hopping of e_g electrons.[2,3] A variety of interesting phenomena in this mixed-valence system like charge ordering of manganese ions, giant oxygen isotope effect, formation of microscopic or macroscopic regions possessing different electronic properties, stimulated development of the DE model itself and inclusion of the electron-phonon interaction.[4–7] The low-temperature state of the manganites corresponds to a ferromagnetic (FM) metal or antiferromagnetic (AFM) insulator with a tendency to-

ward charge ordering of manganese ions $\text{Mn}^{3+}/\text{Mn}^{4+}$. The particular state depends on the hole-doping level x, i.e., on the formal proportion of $\text{Mn}^{3+}/\text{Mn}^{4+}$, and on the relation between the Mn-O and A-O bond lengths and A-O-A bond angles that in turn depend on the average A cation radius $\langle r_A \rangle$. The $(\text{La}_{1-y}\text{Pr}_y)_{0.7}\text{Ca}_{0.3}\text{MnO}_3$ family (hereafter LPCM-100y) has fixed optimal hole doping $x = 0.3$ and variable $\langle r_A \rangle$ that is linearly connected with the Pr concentration y. A detailed study[8] of the manganites with fixed hole doping $A_{0.7}A'_{0.3}\text{MnO}_3$ showed the direct relationship between the Curie temperature T_C and $\langle r_A \rangle$ for a variety of different A,A' cations. It is believed that the principal effect of decreasing $\langle r_A \rangle$ is a decrease in the electron-hopping amplitude between Mn ions (or carriers bandwidth W),[9] which is proportional to T_C in the DE model. The effect of disorder due to size differences between A cations was addressed in Ref. 10. The authors have shown that the metal-insulator transition temperature T_C in the $A_{0.7}A'_{0.3}\text{MnO}_3$ manganites with

fixed $\langle r_A \rangle = 1.23$ Å decreases by $\Delta T_C \propto \sigma^2$, where σ^2 is the dispersion of the A-cation radius r_A. These disorder effects are negligible for $\langle r_A \rangle < 1.22$ Å when the A-cation variance is small and the true variation of T_C with $\langle r_A \rangle$ is observed. In the $(La_{1-y}Pr_y)_{0.7}Ca_{0.3}MnO_3$ series the average radius $\langle r_A \rangle$ is less than 1.206 Å. The r_A dispersion is smaller than 0.000 32 Å^2 for all y, which is in turn significantly smaller than the values of the A cation radius dispersions that affect T_C.[10] Hereafter we use tabulated radii from Ref. 11 assuming ninefold coordination of the A cations. Thus, the LPCM series is a very suitable candidate for the systematic study of the effects caused solely by the variation of the average radius $\langle r_A \rangle$; however, the effects of disorder can still manifest themselves near the metal-insulator boundary, as shown in the numerical Monte Carlo calculations.[12]

The magnetic and crystal structures of the $(La_{1-y}Pr_y)_{0.7}Ca_{0.3}MnO_3$ are well known for the $y=0$ (ferromagnetic, metallic)[13,14] and $y=1$ (canted antiferromagnetic, insulating).[15–17] The metal-insulator (M-I) boundary lays around the Pr concentration $y=0.8$. Near the M-I boundary the low-temperature state can be easily switched from the ferromagnetic metal to insulating antiferromagnet even by a relatively weak effect of the ^{16}O-^{18}O oxygen isotope substitution.[18,19] The magnetic structure of the composition with $y=0.75$ in the vicinity of the M-I transition has been studied by neutron diffraction in Ref. 19. The temperature behavior of the intensities of the charge ordered (CO) and AFM peaks could be interpreted in favor of phase separation onto AFM-insulating and FM-metallic phases at low temperature, though no direct indications of the inhomogeneous state were found. A direct evidence of the percolate phase separation into submicrometer-scale mixture of charge-ordered insulating and ferromagnetic metallic domains has been obtained using electron microscopy data[20,21] in the similar series $La_{5/8-y}Pr_yCa_{3/8}MnO_3$.

We have undertaken a systematic powder neutron diffraction study of the magnetic and structural properties of the $(La_{1-y}Pr_y)_{0.7}Ca_{0.3}MnO_3$ series in the wide range of $\langle r_A \rangle$ with $y=0.6, 0.7, 0.75, 0.8, 0.9, 1.0$ with a special attention given to the question of the homogeneity of the magnetic state near the metal-insulator boundary.

II. SAMPLES: EXPERIMENT

The powder samples for neutron diffraction experiments were prepared by means of the so-called ''paper synthesis'' technique. An aqueous solution of a mixture of La, Pr, Ca, and Mn nitrates taken in the required ratios was deposited on ash-free paper filters, which were dried ($120\,°C$) and then burnt. The oxide product thus obtained was annealed in air at $700\,°C$ for 2 h. The final thermal treatment consisted of annealing pressed pellets in air at $1200\,°C$ for 12 h. Then the pellets were ground. One sample (labeled $P1, y=0.75$) was prepared by the standard solid-state reaction in form of a sintered pellet for the experiment in external magnetic field. The data on the magnetic ordering were obtained by means of the DMC powder diffractometer situated at a supermirror-coated guide for cold neutrons at the Swiss spallation neutron source SINQ (Villigen).[22] The DMC instrument allows

one to carry out simultaneous measurements within a scattering angle range of 80° (angular separation 0.2°). The neutron wavelength range is 2.3–5.5 Å. The measurements were performed by means of an evacuated vanadium pot equipped with a closed-cycle He refrigerator. A helium cryostat equipped with a superconducting magnet was used for the experiments in the external magnetic fields up to 4 T. An oscillating radial collimator suppresses Bragg peaks from the sample environment. The refinements of powder neutron diffraction patterns were made by means of the program FULLPROF,[23] using the internal tables of neutron scattering lengths and magnetic form factors. The nuclear structure of the same samples studied at the high-resolution Fourier time-of-flight diffractometer HRFD (Dubna) provides a complementary information on the coupling between structural and magnetic/electronic properties. The detailed structural data are published elsewhere.[24]

III. MAGNETIC STRUCTURE

The Néel and Curie transition temperatures and the low-temperature magnetic moments in the studied samples are compiled in the Table I. Decreasing the temperature there are subsequent antiferromagnetic (AFM) and ferromagnetic (FM) transitions that are revealed as two sets of the Bragg peaks, e.g., (0 0 1/2), (1/2 0 1/2) for the AFM structure and (101)/(020) for the FM one. A typical neutron diffraction pattern from the LPCM-75 sample ($y=0.75$) is shown in Fig. 1. The nuclear structure has $Pnma$ space group with the lattice parameters $a=5.457$ Å, $b=7.693$ Å, $c=5.448$ Å for the LPCM-75 at room temperature. The Mn atoms occupy the $4b$ position with the coordinates $(0, y, 1/2)$ and $(1/2, y, 0)$, where $y=1,1/2$. The basic antiferromagnetic structure is pseudo-CE (PCE), according to the classification of Refs. 13 and 16. The CE-structure has two propagation vectors $k_1 = [0\ 0\ 1/2]$ and $k_2 = [1/2\ 0\ 1/2]$, corresponding to different Mn sublattices: one (AFM1) for Mn ions in $(0\ y\ 1/2)$, the second one (AFM2) for Mn ions in $(1/2\ y\ 0)$. For the manganites with the electron doping level $x=0.5$ (the ratio $Mn^{3+}/Mn^{4+}=1$) this type of structure is related to the charge ordering of the Mn atoms.[25] The Mn moments are coupled antiferromagnetically in the neighboring layers along b axis in the CE structure, whereas in pseudo-CE structure the layers are aligned ferromagnetically, so that the moment directions of the atoms with coordinates $(x, 0, z)$ and $(x, 1/2, z)$ are the same (Fig. 2). This spin configuration gives magnetic Bragg peaks such as (0 0 1/2), (1/2 0 1/2). The directions of the PCE-component and FM component of the Mn magnetic moments along b axis and c axis, respectively, give the best χ^2 fit for the experimental diffraction patterns. The data on the basic magnetic structure in the LPCM-75 sample were published in our paper on the isotope effect.[19] The magnetic moments of the AFM structure in Ref. 19 are $\sqrt{2}$ times less, because a one-sublattice model was used, which contained two times more magnetic atoms for each propagation vector.

There is a relatively small contribution of an AFM structure revealed as a Bragg peak at $2\theta \simeq 27°$. This peak can be indexed as (1/2 1 1/2) if it is assigned to the propagation

TABLE I. The magnetic moments at $T = 15$ K and the Néel T_N and Curie T_C transition temperatures of the $(La_{1-y}Pr_y)_{0.7}Ca_{0.3}MnO_3$. The values of the moments are given in μ_B. The magnetic moments of the pseudo-CE antiferromagnetic component are μ_{A1} and μ_{A2} for the propagation vectors $k_1 = [0\ 0\ 1/2]$ and $k_2 = [1/2\ 0\ 1/2]$, respectively. μ_F is the moment of the FM phase for $y \leqslant y_{c1}$ and it is the FM component of the canted FM phase in the phase separation region. While for $y > y_{c2}$ it is the canting FM component of the CAF phase. μ_C is the C-type antiferromagnetic component that appears concomitantly with the ferromagnetic moment below T_C. μ_{Pr} shows magnetic moment of Pr ion. For concentrations $y \leqslant 0.6$ no magnetic ordering of Pr ions was detected.

| Sample	y	T_N	T_C	μ_{A1}	μ_{A2}	μ_F	μ_C	μ_{Pr}
LPCM-50 (Ref. 26)	0.5		170(5)			3.40(5)		
LPCM-60	0.6	150(5)	150(5)	0.3(3)	0.0(3)	3.40(6)	0.0(3)	0.01(8)
LPCM-70	0.7	145(5)	130(5)	0.54(7)	0.51(8)	3.32(4)	0.24(8)	0.31(7)
LPCM-75(O16)	0.75	145(5)	115(5)	1.02(5)	0.98(7)	3.32(5)	0.26(8)	0.37(7)
LPCM-75(P1)	0.75	145(5)	115(5)	0.49(12)	0.43(14)	3.42(7)	0.26(12)	0.36(10)
LPCM-80	0.8	130(5)	100(5)	0.79(5)	0.76(7)	3.36(4)	0.26(7)	0.35(5)
LPCM-90	0.9	130(5)	100(5)	1.98(4)	1.96(11)	1.55(6)	0.15(12)	0.22(7)
LPCM-100	1.0	130(1)	110(1)	1.34(5)	1.32(10)	2.15(7)	0.11(25)	0.26(7)
LPCM-O18	0.75	145(5)		2.63(4)	2.63(4)	0	0	0
Yoshizawa *et al.* (Ref. 17)	1.0	140	110	1.4(2)		1.9(2)		
Cox *et al.* (Ref. 15)	1.0	140	120	1.48(2)	1.53(2)	2.20(2)		0.45(2)
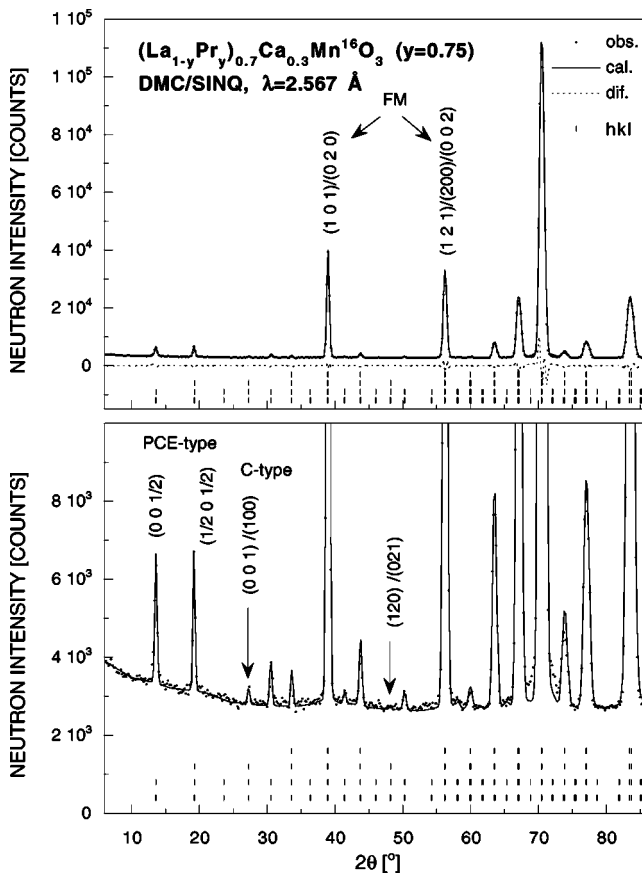
FIG. 1. An example of the Rietveld refinement pattern and difference plot of the neutron diffraction data (DMC/SINQ) for the LPCM-75 sample at $T = 15$ K. The bottom figure shows the same pattern in an enlarged y scale. The top row of the indexing shows the nuclear phase. Next rows are FM+C structure and two AFM sublattices for the PCE-type structure. The peak (0 0 1) can also be indexed as (1/2 1 1/2) and the peak (1 2 0) can be indexed as (3/2 1 1/2). See the text for the details.

vector k_2 of the CE-type structure, but examination of the (0 1 1/2)-type peaks shows the absence of the component with the propagation vector k_1. The most appropriate magnetic moment direction is parallel to the (ac) plane, since no considerable intensity is observed in the peak (1/2 1 3/2) (the refined value amounts to $0.4\mu_B$). Alternatively, this extra peak at $2\theta \simeq 27°$ can also be indexed as (1 0 0)/(0 0 1) because the d-spacing difference between (1/2 1 1/2) and (1 0 0)/(0 0 1) peaks amounts to $\Delta d/d \simeq 10^{-3}$, which is beyond the instrument resolution. According to the Wollan and Koehler classification[13] it corresponds to a C-type antiferromagnetic structure, which has the propagation vector $k = 0$, and the Mn spins in the positions (0 y 1/2) and (1/2 y 0) are antiparallel. The onset temperature of the C structure always coincides, as it is shown below, with the Curie temperature. Thus we associate this additional peak with the ferromagnetic phase. According to the peak intensity ratio the magnetic moments of the C phase cannot lie in the (ac) plane, like in the dominant FM phase, because no considerable intensity is observed in (120)/(021) peak (see Fig. 1). The refined magnetic moment is about $0.25\mu_B$ parallel to b axis. This C component is found only for the compositions $y > 0.6$, i.e., when the ferromagnetic FM phase arises below the Néel temperature on cooling. Thus, the FM phase is noncollinear, but neighboring Mn ions in the positions (0 y 1/2) and (1/2 y 0) form an angle of about 9° (see Table I). In all the compositions revealing antiferromagnetic PCE structure ($y \geqslant 0.6$) the appearance of weak superlattice reflections of (3/2 0 2) type precedes AFM ordering. The appearance of these reflections is believed to be connected to the charge ordering of Mn^{3+}/Mn^{4+} cations, leading to the doubling of the a axis and lowering of the symmetry to the monoclinic $P2_1/m$ space group. The temperature behavior is similar to that of the LPCM-75(O16) and LPCM-O18 sample.[19]

In addition to the ordering of the Mn spins there is a ferromagnetic contribution from the Pr sublattice for the
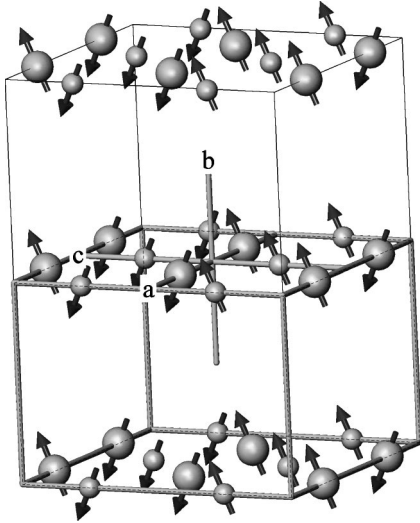
FIG. 2. The homogeneous magnetic structure of Mn ions in the $(La_{1-y}Pr_y)_{0.7}Ca_{0.3}MnO_3$ $(y>0.8)$. The thick lines show $2a \times (b/2) \times 2c$ volume. The ferromagnetic component is directed along c axis. The AFM component has pseudo-CE structure with two Mn sublattices: one (AFM1) for Mn ions in $(0\ y\ 1/2)$ position with the propagation vector $k_1=[0\ 0\ 1/2]$ (shown as small atoms) and the second one (AFM2) for Mn ions in $(1/2\ y\ 0)$ with $k_2 =[1/2\ 0\ 1/2]$ (shown as large atoms). The antiferromagnetic component is directed along the b axis. In the phase separated state the FM and AFM components are not superimposed, but spatially separated forming collinear antiferromagnetic PCE and FM regions. Minor canting of the FM component due to appearance of C-type structure (see the text for the details) below T_C is not shown.

compositions with sufficiently large Pr concentration y >0.6. This is clearly seen from the disproportion of the intensities between the $(101)/(020)$ and $(121)/(002)$ peaks if one assumes only Mn ordering. The Pr ferromagnetism is revealed as a small decrease in the integrated intensity of $(101)/(020)$ peak on cooling (see Figs. 5 and 6), because the structure factor of this peak for the Pr sublattice is negative with respect to the Mn one. The direction of the Pr moments is parallel to the Mn moments in the FM phase and thus presumably induced by Mn. The low-temperature values of the moments are listed in Table I. Indeed the moment of Pr scales with the ferromagnetic component of Mn moment rather than with the Pr concentration.

A. Temperature and field dependence of the magnetic Bragg peaks

The temperature evolution of the neutron diffraction patterns from the LPCM-80 sample that is typical for $y=0.6$ -0.8 is shown in Fig. 3. One can see the appearance of the antiferromagnetic Bragg peaks below Néel temperature T_N $=130$ K and the increase in the nuclear peaks below Curie temperature $T_C=100$ K. We found that the $(La_{1-y}Pr_y)_{0.7}Ca_{0.3}MnO_3$ series has three distinct types of behavior of the magnetic structure, which are separated by two critical Pr concentrations $y_{c1}=0.6$ and $y_{c2}=0.85$, as shown in the phase diagram in Fig. 4.
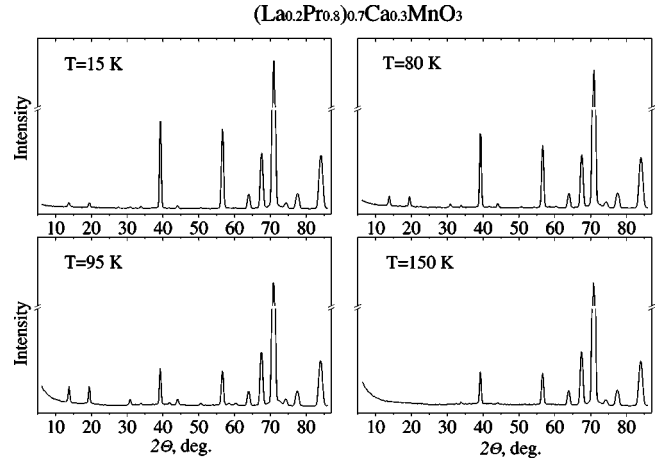

FIG. 3. Typical neutron diffraction patterns from the LPCM-80 sample for several temperatures measured with $\lambda=2.567$ Å. One can see the sharp increase in the Bragg peak intensities $(101)/(020)$ at $2\theta=38.6°$ and $(121)/(020)$ at $2\theta=55.8°$, connected with ferromagnetic ordering and appearance of the antiferromagnetic Bragg peaks $(0\ 0\ 1/2)$ and $(1/2\ 0\ 1/2)$ around $13.5°$ and $19.2°$. Also an increased background at small 2θ is seen at high temperatures due to diffuse paramagnetic scattering.

Below y_{c1}, corresponding to the A-cation radius $\langle r_A \rangle$ $\simeq 1.19$ Å, the magnetic state is a collinear ferromagnetic
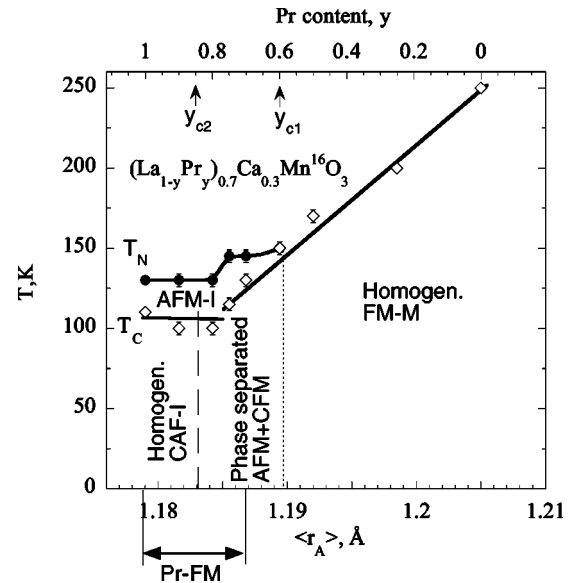

FIG. 4. Phase diagram of the $(La_{1-y}Pr_y)_{0.7}Ca_{0.3}MnO_3$. The diamonds and circles show the ferromagnetic T_C and antiferromagnetic T_N ordering temperatures of the Mn spins. The bottom x axis shows average A cation radius $\langle r_A \rangle$. The low-temperature state is homogeneous for $y>0.8$ (canted antiferromagnetic insulator CAF-I) and for $y<0.6$ (ferromagnetic metal FM-M). In the range $0.6 \leq y \leq 0.8$ the magnetic state is inhomogeneous mixture of slightly canted ferromagnetic (CFM) and AFM regions. The antiferromagnetic T_N and ferromagnetic T_C transition temperatures coincide for $y=0.6$. The data for $y=0$ and $y=0.25$ are from Refs. 14 and 9. A ferromagnetic contribution of Pr moments is found in the interval of the Pr concentration marked as Pr-FM.
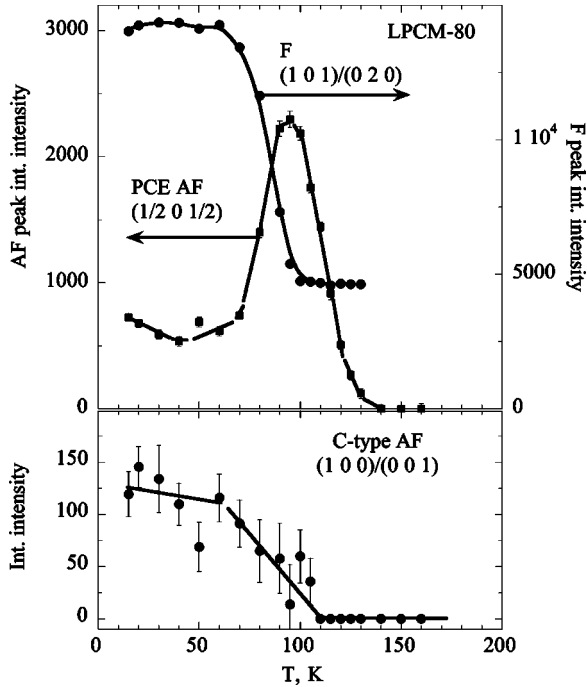
FIG. 5. Temperature dependence of the integrated intensities of the characteristic diffraction peaks in the LPCM-80. Top: ferromagnetic peak (101)/(020) and antiferromagnetic peak (1/2 0 1/2) corresponding to the propagation vector [1/2 0 1/2] of the PCE structure. Temperature dependence of the (0 0 1/2) peak is similar to the (1/2 0 1/2) one. Bottom: Integrated intensity of the (100)/(001) peak, corresponding to C-type magnetic structure, which is coupled to FM component. The lines are guides to the eye.
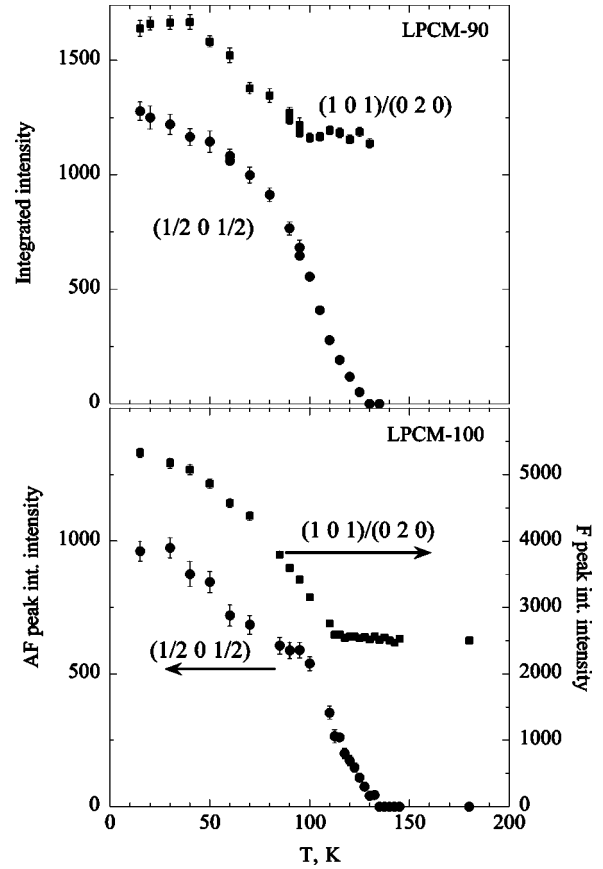

FIG. 6. Temperature dependence of the integrated intensities of the characteristic ferromagnetic (101)/(020) and antiferromagnetic (1/2 0 1/2) diffraction peaks in the LPCM-90 (top) and LPCM-100 (bottom). Temperature dependence of the (0 0 1/2) peak is similar to the (1/2 0 1/2) one.

one[9,26] in accordance with the phase diagram of Ref. 8. The temperature dependence of the ordered magnetic moment for $y = 0.5$ is given in Ref. 26.

In the range $y > y_{c1}$ the antiferromagnetic component appears. The sample first undergoes the AFM transition to a PCE structure followed by transition to the ferromagnetic phase, which becomes the dominant phase at low temperature. The Néel temperature is preceded by charge ordering at higher temperature of about 180 K.[15,19] Figure 5 shows the integrated intensities for the characteristic magnetic diffraction peaks of the LPCM-80 sample as a function of temperature. One sees that the temperature dependence of AFM-peak intensities are nonmonotonous, but with a well-defined maximum near the Curie temperature T_C. This kind of temperature dependence was observed in all the samples in the range $y_{c1} < y < y_{c2}$. The maximum in the AFM intensity can be understood in frame of a phase-separated state when the FM phase grows spatially separated from the AFM host. The reduction of the volume occupied by the AFM phase is revealed as a decrease in the corresponding Bragg peak intensity. Alternatively, the ferromagnetic component can appear as a result of the canting of the AFM moments below T_C, provided that the total magnetic moment is preserved. The question of the homogeneity of the low-temperature magnetic state cannot be resolved from the neutron diffraction pattern in zero external magnetic field.

For the compositions with $y > y_{c2}$ the temperature dependence of the magnetic peaks are significantly different (Fig. 6). The AFM intensity has no maximum with temperature lowering, and the ferromagnetism is not a dominating state at low temperature. We note, that the magnetic behavior of the ^{18}O-enriched sample[19] ($y = 0.75$) is similar to one observed for the natural-oxygen-containing samples with $y > y_{c2}$.

To access the question of the homogeneity of the low-temperature magnetic state, we have performed the neutron diffraction experiments in an external magnetic field directed perpendicular to the scattering plane. The effect of the external magnetic field on the magnetic structure of manganites was first studied in the classical paper by Wollan and Koehler.[13] To avoid possible reorientation of the ferromagnetic crystallites in the high magnetic field, the samples were made as a ceramic pellet [LPCM-75(P1) sample] or as pressed pellets of the powders measured in the zero external field (LPCM-80 and LPCM-90 samples). Figure 7 shows the integrated intensities of the characteristic magnetic diffraction peaks of the LPCM-75(P1), LPCM-80, and LPCM-90 samples as a function of the external magnetic field. If the AFM and FM components are coupled forming the CAF homogeneous structure one expects that an increase in FM peak intensity should be accompanied by a decrease in AFM
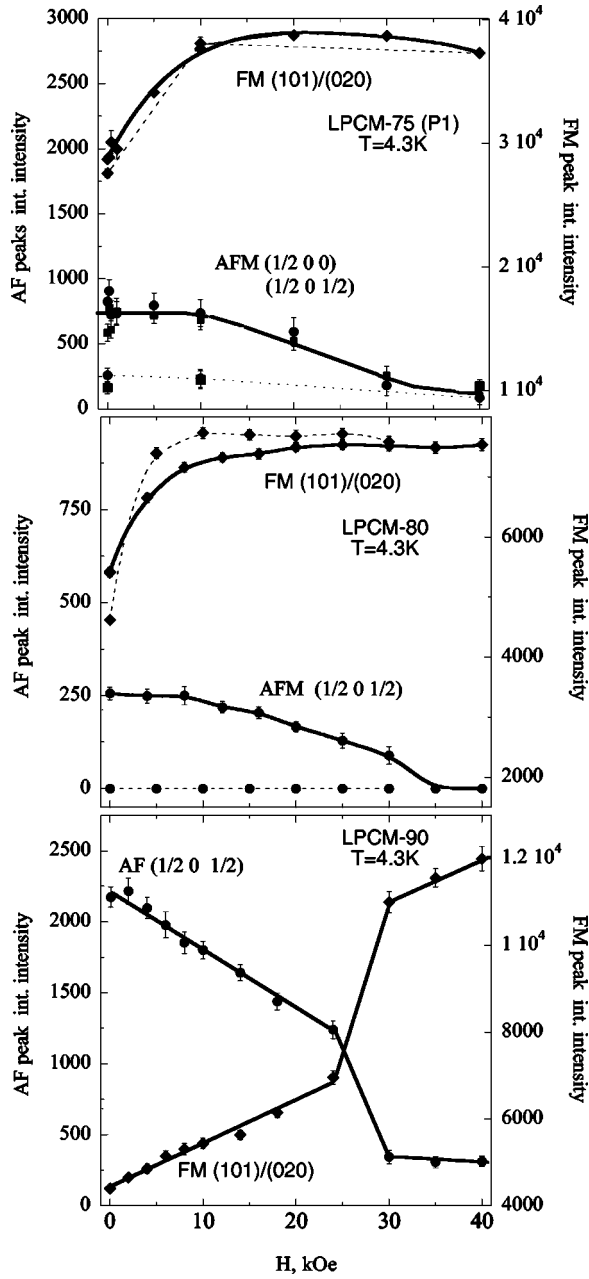
FIG. 7. The integrated intensities of the characteristic antiferromagnetic (1/2 0 1/2), (0 0 1/2) and ferromagnetic (101)/(020) diffraction peaks of the LPCM-75P1, LPCM-80, and LPCM-90 samples as function of the external magnetic field. The lines are guides to the eye. The increasing and decreasing field scans are marked by solid and dashed lines, respectively.

ones. In the experiment with the samples LPCM-75(P1) and LPCM-80 the AFM intensities stay constant, while the FM one is increased until 10 kOe. This means that the FM moment is decoupled from AFM one, being spatially separated. The increase in FM peaks occurs due to the increase in the magnetic structure factor $F_m^2 \sim m^2 - (\mathbf{qm})^2$, when the FM moments $\mathbf{m}$ turn perpendicular to the scattering vector $\mathbf{q}$ resulting from the application of the external field. At higher external fields $H > 10$ kOe the AFM state melts as it is usually observed in manganites, because the gain in Zeeman
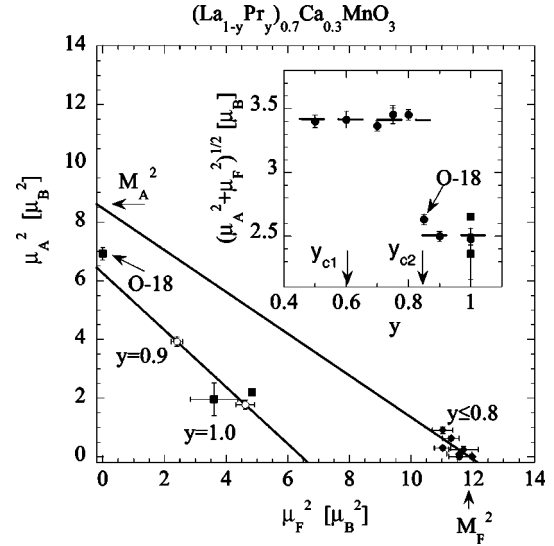

FIG. 8. The square of the antiferromagnetic (*A*) magnetic moment component μ_A^2 as a function of the square of the ferromagnetic (FM) magnetic moment component μ_F^2 with Pr concentration y as a parameter. The circles show our data, the squares for the concentration $y = 1.0$ are taken from the literature (see Table I, where the moment values are compiled). One can distinguish two different linear slopes and the values of moments. The lines are the linear LS fits to the data points for $y \leq 0.8$ and $y \geq 0.9$. The point for ^{18}O-enriched sample ($y = 0.75$) is also shown (O-18). It has no FM component at all, serving as a reference of pure antiferromagnetic state. The inset shows the total magnetic moment $\mu_A^2 + \mu_F^2$ as a function of the Pr concentration. The O-18 sample was assigned the Pr concentration $y = 0.85$.

energy stabilizes the ferromagnetic metallic state. Reducing the external field to zero does not restore the AFM state: the sample remains in the metallic ferromagnetic state. In the sample LPCM-90 that has $y > y_{c2}$ the AFM and FM intensities are synchronously changed as a function of the external field (Fig. 7), implying that AFM and FM components are indeed coupled forming a canted antiferromagnetic structure.

B. Low-temperature magnetic moments

In the region $y < y_{c2}$ the magnetic state at low temperature is predominantly ferromagnetic. When the Pr concentration is increased above y_{c1} the AFM component appears, but the FM moment remains large and is not decreased very much when the concentration y is increased. However, when the concentration exceeds $y = y_{c2}$ the magnetic state changes very significantly. In the plot $\mu_A^2(\mu_F^2)$ (Fig. 8) with the concentration y as a parameter, one can distinguish two different linear slopes and the values of moments—one is for $y \leq 0.8$ and the other for $y = 0.9, 1$. The total ordered magnetic moment undergoes a jump at $y = y_{c2}$, implying that a concentrational first-order phase transition takes place at y_{c2}. In the PS state the $\mu_A^2(\mu_F^2)$ has to be a linear function, provided that the magnetic moments of the phases are not changed inside the two-phase state. Assuming that the phase separation goes into a pure AFM state with magnetic moment M_A and a FM state with a moment M_F, the effectively observed magnetic moments read:

$$\mu_A^2 = M_A^2 - \frac{M_A^2}{M_F^2} \mu_F^2, \qquad (1)$$

where μ_F^2/M_F^2 is the volume fraction of the FM phase. Because of the limited range of the magnetic moments for the concentrations $y \lesssim 0.8$ one can get only a very rough estimate of the AFM moment $M_A = (3 \pm 0.5)\mu_B$, by fitting the data to the formula (1).

A fit of our data for $y \geqslant 0.9$ to the formula (1) yields $M_A = M_F = 3.2\mu_B$, implying that for the homogeneous CAF state the end values of the AFM and FM moments are equal, and an intermediate CAF state is realized by the change in the canting angle. It is worth noting that the magnetic moment of the O-18 sample is in accordance with this value.

IV. BRAGG-PEAK BROADENING EFFECTS

The magnetic-Bragg-peak broadening effects were studied by means of DMC instrument using the neutron wavelength $\lambda = 5.43$ Å. The resolution of the instrument for this wavelength is $\Delta d/d = (0.7-1.8) \times 10^{-2}$ for the d-spacing range from 3.8 Å to 11 Å. This d range was enough to cover both antiferromagnetic peaks (0 0 1/2), (1/2 0 1/2) and the ferromagnetic (101)/(020) peak. The peak-broadening effects are present for both LPCM-100 and LPCM-75 samples being in the homogeneous and the phase-separated regions of the phase diagram, respectively. Figures 9 and 10 show the temperature dependence of the peak widths. In the pure AFM state ($115 < T < 145$ K) the widths correspond to the constant values. Below the Curie temperature both widths start to increase. The FM width is increased much faster than the AFM ones in the LPCM-75 sample. The temperature dependence of the integrated intensities for the LPCM-75 sample are also shown for convenience. The widths in the LPCM-100 sample are systematically larger than in LPCM-75 sample because of the larger diameter of the sample container. The width of the ferromagnetic peak (101)/(020) has a contribution caused by overlapping of the (101) and (020) peaks that have slightly different d spacing. The middle plot of Fig. 9 shows the FM width corrected for the shift in the (101) and (020) peak positions, based on the lattice parameters data measured with the high-resolution neutron diffraction instrument HRFD (IBR2, Dubna).[19,24] The dip in the temperature dependence of the (101)(020) peak width is apparently due to specific temperature dependence of the lattice parameters. However, the increase in the width, which is clearly seen in the middle plot of Fig. 9 is definitely connected with the ferromagnetic transition. There are two basic contributions to the width increase $\Delta(\delta 2\theta)/2\tan(\theta) = [(d/L)^2 + (\delta a/a)^2]^{1/2}$: the finite size of the coherently scattered regions L (size effect) and the dispersion of the lattice parameters ($\delta a/a$) (strain effect). The strain contribution must be present, because the lattice parameters in the ferromagnetic and antiferromagnetic phases are different.[19] If we neglect the strain contribution in the peak width (anyway we cannot separate strain and size effect due to the limited d range) we can estimate the lower limit of the domain sizes $L = d/(\Delta d/d)$ as $>1500(100)$ Å, $>500(100)$ Å, $>700(150)$ Å for the FM, AFM1, and
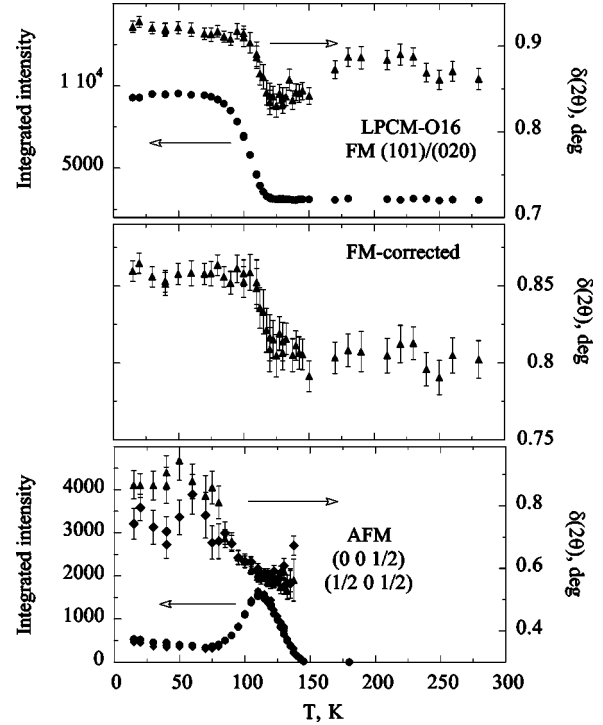

FIG. 9. The FWHM width (right y axis) of the ferromagnetic peak (101)/(020) (top) and antiferromagnetic peaks (0 0 1/2), (1/2 0 1/2) (bottom) measured at DMC/SINQ instrument with wavelength $\lambda = 5.43$ Å for the LPCM-75(O16) sample. The widths are given in 2θ degrees. The plot in the middle shows the ferromagnetic peak width corrected on the broadening caused by overlapping of peaks (101) and (020), which are not resolved. See text for details. The corresponding integrated magnetic peak intensities are also shown (left y axis).

AFM2 phases in the sample LPCM-75, respectively, and $>690(50)$ Å, $>430(50)$ Å, $>520(60)$ Å in the sample LPCM-100 (the error bars represent only statistical errors). The finite regions can occur due to both a plain ferromagnetic domain structure and the phase-separated state. In the first case one would expect the same sizes of the FM and AFM regions because they originate from the homogeneous canted AFM magnetic state. In phase separation scenario, proposed for the LPCM-75 sample, one would expect larger ferromagnetic domains and smaller antiferromagnetic clusters at low temperature, since the ferromagnetic phase occupies about 86% of the sample volume. Experimentally, we can tentatively propose that there is a tendency to this behavior, but this qualitative peak-width analysis cannot be considered as an evidence. More important and reliable consequence of the peak-width analysis is that the domains of the AFM phase are macroscopically large in the phase-separated state, and hence the separation cannot be driven by simple charge separation between FM and AFM regions.

V. DISCUSSION

First, we shall address the topology of the phase separated state. It can be realized as (i) an incoherent mixture of FM and AFM regions, or (ii) a superstructure formed by the
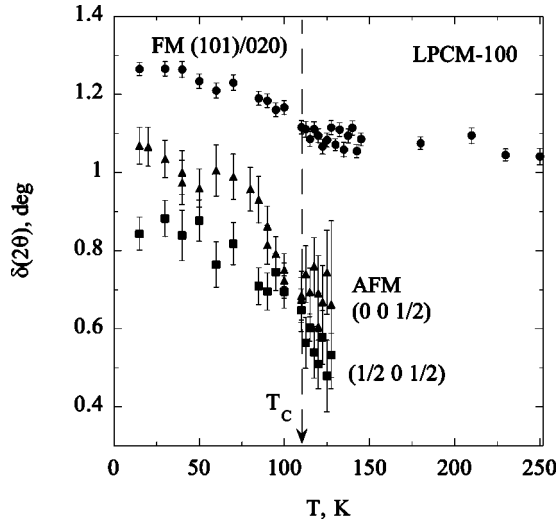
FIG. 10. The FWHM width of the ferromagnetic peak (101)/(020) (top) and antiferromagnetic peaks (0 0 1/2), (1/2 0 1/2) (bottom) measured at DMC/SINQ instrument with wavelength $\lambda = 5.43$ Å for the LPCM-100 sample. The widths are given in 2θ degrees. The corresponding integrated magnetic peak intensities are also shown in Fig. 6.

AFM regions inside the dominating FM phase, e.g., a stripe-like structure. The second choice implies presence of superstructure reflections, presumably incommensurate ones. These extra Bragg peaks have to be coupled to the FM peaks, and appear at T_C when the phase separation begins. A weak Bragg peak, indexed as C-type (100)/(001), which we observe concomitantly with onset of the ferromagnetic ordering, could be a manifestation of such a superstructure, but we failed to find any satellites that would correspond to other nuclear Bragg peaks, assuming an appropriate k vector of this superstructure. Thus, we consider the phase separated state as an incoherent mixture of AFM and FM domains. The sizes of the domains are macroscopically large as shown above. However, there is no clear evidences in favor of the two-phase nuclear model from the high-resolution neutron diffraction data[24] presumably because of very close structure parameters and also peak-broadening effects caused by the internal stresses. The small C-type canting of the FM component is observed only for the samples in the phase-separated region $y_{c1} < y < y_{c2}$, while outside this region the C-type component is practically zero (Table I). A probable origin of this C canting could be the boundaries between the phase-separated regions, where the spins aligned ferromagnetically along c axis are canted along b axis—the axis of the AFM ordering of the neighboring PCE phase.

The total ordered magnetic moment of the Mn ion of $3.4\mu_B$ observed for Pr concentration $y \lesssim 0.8$ is close to the maximal value expected for the average Mn^{3+}/Mn^{4+} spin moment $3.7\mu_B$ for the given hole doping $x = 0.3$. The long-range ordered magnetic moment in the homogeneous CAF phase ($y \geqslant 0.9$) is 26% smaller (see Fig. 8). This implies that only 54% of the sample volume is occupied by the CAF phase assuming the same magnitude of the magnetic moment of $3.4\mu_B$. In this case the magnetic state of the rest of the sample volume does not possess long-range magnetic order.

Thus, spatial inhomogeneities can still be present in the samples with ($y \geqslant 0.9$), but the space between the homogeneous CAF regions is filled with the regions that are either short-range ordered or paramagnetic. In Ref. 27 it was reported that an approximately equal proportion of two distinct crystallographic phases was present in $Pr_{0.7}Ca_{0.3}MnO_3$, revealed as a splitting of the (040)/(202) doublet in the high-resolution neutron diffraction experiment. The second phase observed in Ref. 27 could be related to the magnetically disordered regions. We did not observe similar peak splitting in our sample LPCM-100 in a high-resolution neutron diffraction experiment.[24] The authors of Ref. 27 also note that the peak-splitting effect is sample dependent.

The phase diagram (Fig. 4) of $(La_{1-y}Pr_y)_{0.7}Ca_{0.3}MnO_3$ contains a region of Pr concentrations $y_{c1} < y < y_{c2}$ where the low-temperature magnetic state is an inhomogeneous mixture of two phases. Outside of this region the long-range ordered state is homogeneous ferromagnetic and metallic for $y < 0.6$ or canted antiferromagnetic insulating for $y \geqslant 0.9$. This kind of phase diagram agrees quite well with the conclusions of the Ref. 12, where the computational studies of models for manganese oxides showed the generation of large coexisting metallic and insulating clusters with equal electronic density. The clusters are induced by disorder on exchange and hopping amplitudes near first-order transition. In our case, the increase in the Pr concentration decreases the effective conduction carrier bandwidth $W \propto \sin(\varphi/2)$ via the Mn-O-Mn angle φ (a detailed discussion is given in Ref. 9) which is linearly dependent on the concentration y.[24] Decreasing the width W to a critical value, the state is changed from the metallic ferromagnetic to insulating charge-ordered antiferromagnetic. The critical Pr concentration is around $y \simeq 0.7$ (the middle of the phase-separated region). Since the change in the bandwidth W is realized by changing of the average radius of A cation, via Pr/La substitution, the statistical disorder of the hoping amplitudes is naturally present. The variance of the A-cation radius in $(La_{1-y}Pr_y)_{0.7}Ca_{0.3}MnO_3$ reads $\sigma = \Delta r_A[0.7(1-y)(0.3 + 0.7y)]^{1/2}$, where $\Delta r_A = (r_{Pr} - r_{La})$, the radius of the Ca ion is the same as Pr ion. Near the critical concentration $y = 0.7$ the variance is still quite large, $\sigma = 0.015$ Å, in comparison with the width of the two-phase region 0.007 Å in the $\langle r_A \rangle$ units. The corresponding fluctuations of the local Mn-O-Mn angle can be responsible for the appearance of the clusters as shown in Ref. 12. Near the metal-insulator boundary the phases have very close ground-state energies and can be transformed from one to another by relatively weak effects of a moderate external field or an oxygen isotope substitution. However, the unit-cell volume of the FM phase is 0.15% smaller than in the AFM one, and the values of valence angles and interatomic distances are also significantly different.[24] Importance of internal stresses that must exist in the two-phase state was pointed out in the Ref. 21. Even if the ferromagnetic phase has lower energy, its growth inside the antiferromagnetic host can be suppressed by the stresses on the boundaries with the AFM host, leading to the phase-separated state.

The ^{18}O-isotope substituted sample LPCM-O18 (y = 0.75) reveals the ordered magnetic moment close to the natural isotope samples with ($y \geq 0.9$), but with a zero ferromagnetic component (see Table I, Fig. 8). This places LPCM-O18 in the region above the concentrational transition at $y_{c2} \simeq 0.85$. The LPCM-O18 sample is the sole example of a pure antiferromagnetic insulating state in the $(La_{1-y}Pr_y)_{0.7}Ca_{0.3}MnO_3$ series. The y doping for $y \geq 0.9$ increases the canting angle by increasing the ferromagnetic component (Fig. 8). On the basis of this tendency the LPCM-O18 sample can be assigned to the Pr concentration in the range between $y = 0.8$ and $y = 0.9$. This implies that the renormalization of the charge carrier bandwidth W by substitution of ^{16}O for ^{18}O corresponds to an effective change of Pr concentration by about $\Delta y = 0.1$.

VI. CONCLUSIONS

The magnetic structure of the series $(La_{1-y}Pr_y)_{0.7}Ca_{0.3}MnO_3$ for y from 0.5 to 1.0 has been studied by neutron powder diffraction in the temperature range from 10 to 293 K and in external magnetic fields up to 4 T. At the low Pr content $y = 0.5$ the structure is homogeneous ferromagnetic. For the compositions with $y \geq 0.6$ there is a superposition of the FM and pseudo-CE-type antiferromagnetic (AFM) structures. The magnetic moments of Mn atoms are directed along the c axis and the b axis in the FM and AFM phases, respectively. The temperature and external magnetic field dependencies of the integrated FM- and AFM-peak intensities and the magnetic Bragg-peak widths in the samples with $0.6 \leq y \leq 0.8$ indicate presence of the macroscopic incoherent phase separation into the FM and AFM domains, implying that the CMR effect has a percolation nature in this region of the Pr concentrations. The FM phase has a small noncollinearity (AF component of C type with magnetic moment along b axis), presumably due to interface regions to the AF phase. The spatial dimensions of the phases are large ($\geq 10^3$ Å), and hence the separation cannot be a simple charge segregation.

The total long-range ordered magnetic moment of the Mn ion shows a steplike decrease from $\mu_{Mn} = 3.4 \mu_B$ to $2.5 \mu_B$ as a function of Pr concentration at $y = 0.85$. For the concentrations $y \geq 0.9$ the low-temperature long-range ordered magnetic state is again homogeneous with canted AFM structure of pseudo-CE type. The canting angle is significantly increased on doping, while the total magnetic moment stays constant for $y \geq 0.9$. The ^{18}O isotopic sample with $y = 0.75$ can be considered as an end member of the CAF homogeneous state with zero canting angle. The spatial inhomogeneities can still be present for $y \geq 0.9$ (according to the reduced μ_{Mn} value), but the Mn spins between the homogeneously CAF-ordered moments have to be either short-range ordered or paramagnetic.

Our data show that the phase diagram of $(La_{1-y}Pr_y)_{0.7}Ca_{0.3}MnO_3$ has border region of Pr concentrations $0.6 \leq y \leq 0.8$, where the low-temperature magnetic state is macroscopically inhomogeneous. The presence of this border between the homogeneous CAF insulating and FM metallic states can be understood in frame of computational studies of models for manganese oxides.[12] The macroscopical clusters can be induced by disorder on the carriers hopping amplitude caused by natural dispersion of the A cation radius (and, hence, Mn-O-Mn bond angles) near the first-order metal-insulator transition around $y = 0.7$. Additional factor stabilizing the phase-separated state is inhomogeneous stresses near the phase boundaries that occur due to mismatch of the crystal structures of the ferromagnetic and antiferromagnetic phases.

*Corresponding author. Present address: Frank Laboratory of Neutron Physics, Joint Institute for Nuclear Research, 141980 Dubna, Russia.

[1] S. Jin, M. McCormack, T.H. Tiefel, and R. Ramesh, J. Appl. Phys. **76**, 6929 (1994).

[2] P.W. Anderson and H. Hasegawa, Phys. Rev. **100**, 675 (1955).

[3] P.G. de Gennes, Phys. Rev. **118**, 141 (1960).

[4] A.J. Millis, Nature (London) **392**, 147 (1998).

[5] M.Yu. Kagan, D.I. Khomski, and M.V. Mostovoy, Eur. Phys. J. B **12**, 217 (1999).

[6] E.L. Nagaev, Phys. Rev. B **60**, 455 (1999).

[7] A.S. Alexandrov and A.M. Bratkovsky, Phys. Rev. Lett. **82**, 141 (1999).

[8] H.Y. Hwang, S.-W. Cheong, P.G. Radaelli, M. Marezio, and B. Batlogg, Phys. Rev. Lett. **75**, 914 (1995).

[9] P.G. Radaelli, G. Iannone, M. Marezio, H.Y. Hwang, S.-W. Cheong, J.D. Jorgensen, and D.N. Argyriou, Phys. Rev. B **56**, 8265 (1997).

[10] L.M. Rodriguez-Martinez and J.P. Attfield, Phys. Rev. B **54**, 15 622 (1996).

[11] R.D. Shannon, Acta Crystallogr. **32**, 751 (1976).

[12] A. Moreo, M. Mayr, A. Feiguin, S. Yunoki, and E. Dagotto, Phys. Rev. Lett. **84**, 5568 (2000).

[13] E.O. Wollan and W.C. Koehler, Phys. Rev. **100**, 545 (1955).

[14] Q. Huang, A. Santoro, J.W. Lynn, R.W. Erwin, J.A. Borchers, J.L. Peng, K. Ghosh, and R.L. Greene, Phys. Rev. B **58**, 2684 (1998).

[15] D. Cox, P.G. Radaelli, M. Marezio, and S.-W. Cheong, Phys. Rev. B **57**, 3305 (1998).

[16] Z. Jirak, S. Krupicka, Z. Simsa, M. Dlouha, and S. Vratislav, J. Magn. Magn. Mater. **53**, 153 (1985).

[17] H. Yoshizawa, H. Kawano, Y. Tomioka, and Y. Tokura, Phys. Rev. B **52**, 13 145 (1995).

[18] N.A. Babushkina, L.M. Belova, O.Yu. Gorbenko, A.R. Kaul, A.A. Bosak, V.I. Ozhogin, and K.I. Kugel, Nature (London) **391**, 159 (1998).

[19] A.M. Balagurov, V.Yu. Pomjakushin, D.V. Sheptyakov, V.L. Aksenov, N.A. Babushkina, L.M. Belova, A.H. Taldenkov, A.V. Inyushkin, P. Fischer, M. Gutmann, L. Keller, O.Yu. Gorbenko, and A.R. Kaul, Phys. Rev. B **60**, 383 (1999).

[20] M. Uehara, S. Mori, C.H. Chen, and S.-W. Cheong, Nature (London) **399**, 560 (1999).

[21] P. Littlewood, Nature (London) **399**, 529 (1999).

[22] P. Fischer, L. Keller, J. Scheffer, and J. Kohlbrecher, Neutron News **11**, 19 (2000).

[23] J. Rodrigues-Carvajal, Physica B **192**, 55 (1993).

[24] A.M. Balagurov, V.Yu. Pomjakushin, D.V. Sheptyakov, V.L. Aksenov, N.A. Babushkina, L.M. Belova, O.Yu. Gorbenko, and A.R. Kaul, Eur. Phys. J. B **19**, 215 (2001).

[25] J.B. Goodenough, Phys. Rev. **100**, 564 (1955).

[26] A.M. Balagurov, V.Yu. Pomjakushin, V.L. Aksenov, N.M. Plakida, N.A. Babushkina, L.M. Belova, O.Yu. Gorbenko, A.R. Kaul, P. Fischer, M. Gutmann, and L. Keller, Pis'ma Zh. Éksp. Teor. Fiz. **67**, 672 (1998) [JETP Lett. **67**, 705 (1998)].

[27] P. Radaelli, R.M. Ibberson, S.-W. Cheong, and J.F. Mitchell, Physica B **276-278**, 551 (2000).